The far wake of porous disks and a model wind turbine: Similarities and differences assessed by hot-wire anemometry

Magnus K. Vinnes, Stefano Gambuzza, Bharathram Ganapathisubramani, et al.

The far wake of porous disks and a model wind turbine: Similarities and differences assessed by hot-wire anemometry

View Online   Export Citation   CrossMark

Magnus K. Vinnes,[1,a] (iD) Stefano Gambuzza,[2] (iD) Bharathram Ganapathisubramani,[2] (iD) and R. Jason Hearst[1,a] (iD)

AFFILIATIONS

[1]Department of Energy and Process Engineering, Norwegian University of Science and Technology, Trondheim, Norway
[2]Engineering and Physical Sciences, University of Southampton, Southampton, United Kingdom

[a]Authors to whom correspondence should be addressed: magnus.kyrkjebo@ntnu.no and jason.hearst@ntnu.no

ABSTRACT

The wakes of two different porous disks have been evaluated experimentally. Such disks are commonly used as physical actuator disk analogs for wind turbines. One disk is made of a uniform wire mesh, while the other has a nonuniform design with radial spars connected by rings. The disks have the same solidity and produce approximately the same drag. The wakes have also been compared to the wake of a model wind turbine and a solid disk. In contrast to earlier studies, the far wake, up to 30 diameters downstream, is included in the comparison. In the near wake, the velocity deficit and turbulence intensity profiles of the disk wakes differ significantly. High levels of turbulence intensity in the wake of the nonuniform disk increase the transverse transport in the wake, which leads to faster spreading and lower velocity deficits in the far wake, compared to the uniform disk and the wind turbine. High velocity gradients in the wake of the uniform disk give rise to turbulence production farther downstream, maintaining higher turbulence levels in the far wake. In addition, coherent vortex shedding is only identified in the wake of the nonuniform disk. None of the disks were able to replicate the asymmetric features of the wind turbine wake. Nonetheless, the results highlight important flow physics that should be considered in the design process of a porous disk used as a wind turbine surrogate.

I. INTRODUCTION

Wind turbines (WTs) are typically located in clusters, called wind farms. In such farms, many turbines operate in the wake of upstream turbines, experiencing reduced mean wind velocity and increased turbulence intensity (TI) compared to the undisturbed incoming flow. The decreased velocity reduces the power production potential. Barthelmie and Jensen[1] found a difference in the power production of up to 20% between turbines located in the center of the Nysted offshore wind farm and the turbines located at the edge. Increased TI leads to higher mechanical loads on the structure. Thomsen and Sørensen[2] reported 5%–15% higher loads on a turbine in a farm compared to a single turbine, with the exact value depending on the farm layout.

The near wake is often defined to be the region where rotation and tip and root vortices are seen in the flow, that is, where the signature of the turbine, nacelle, and tower dominate the flow.[3] The near wake of a wind turbine is a highly three-dimensional flow. The turbine rotation adds a counter-rotation to the wake flow.[4] Tip vortices and root vortices further complicate the flow.[3,5] However, both the rotation and the vortices lose strength rapidly. The azimuthal velocity in the wake has been shown to be only a few percent of the freestream velocity at a distance of 1 rotor diameter (D) downstream of the turbine.[4] The size of the near wake depends on the incoming flow. Typically, it ends between $2D$ and $4D$ downstream of the turbine.[6,7]

In wind farms, the spacing between turbines is typically in the range of $5D$ to $10D$, as exemplified by five different full scale farms shown in Table I. Depending on the wind direction compared to the farm alignment, turbines even farther downstream might be located directly in the wakes of upstream turbines, as can be seen in the work by Porté-Agel *et al.*[8] The turbines will thus never be located in the near wake of other turbines, but rather in the far wake. While the flow is highly three dimensional in the near wake, the far wake has more global characteristics of the velocity deficit and TI.[3] When the complicated flow structures in the near wake are less important, it is possible

TABLE I. Turbine spacing in different wind farms.

Wind farm	Spacing (D)
Nysted[1]	5.8–10.5
Horns rev I[13]	7
Rødsand II[14]	5–10
Greater Gabbard[15]	8.3–10
Princess Amalia[16]	6.9–7.1

to simplify both computations and experiments. Therefore, actuator disk (AD) methodology has become a popular tool. In simulations, it consists of implementing a pressure discontinuity at the disk location.[9] In some cases, the rotation of the flow can also be added.[7,10,11] In experiments, the analogy is to use porous disks (PDs) with the same drag coefficient

$$C_D = \frac{F_D}{\frac{1}{2}\rho U_\infty^2 A} \quad (1)$$

as that of a wind turbine.[12] Here, F_D is the drag force acting on the turbine; ρ is the density of the air; U_∞ is the freestream velocity; and A is the swept area of the rotor, corresponding to the frontal area of an AD. Note that in this study, C_D is used rather than the thrust coefficient C_T, as the focus is on disks. They are, however, the same parameter.

Computational research has evolved to utilize the available computational power of supercomputers. Large eddy simulations (LESs), where only the small turbulent scales are modeled and the large scales are directly simulated from the governing equations, have become a popular tool. Many LES studies on wind turbines or wind farms utilize either rotating or non-rotating AD models (e.g., Refs. 8 and 17–20). Reviews on simulations of wind farm flows are found in the recent review papers by Stevens and Meneveau[6] and Porté-Agel et al.[7] In industrial applications, where LES is too expensive, wake models are used to plan the layout of a wind farm. Some of the best known models are the Jensen model[21] and the Frandsen model.[22] The development of new wake models as well as the improvement of earlier models are still subjects of academic interest.[23–26] Experimental studies are needed to validate both wake models and simulation results,[6] and are also useful and necessary to obtain further insight into the physical phenomena that govern flow around wind turbines and wind farms.[7]

PDs are popular to use as experimental wind turbine models. Wake meandering in relation to large scale boundary layer structures was investigated by España et al.[27,28] and Muller et al.,[29] who both used wire mesh disks as a static wind turbine models. Howland et al.[30] studied the wake deflection downstream of a yawed PD, stating that the deflection of the wake is largest near the center. They used a disk with ribs protruding from the center, connecting several solid circles at different radial positions. Very recently, Abdulrahim et al.[31] investigated which effects an incoming boundary layer has on the wake of a PD of similar design. Unsteady loading on wire mesh disks was studied by Yu et al.[32,33] PDs have also been used as wind turbine models in wind farm experiments. For example, Theunissen et al.[34] measured

the drag of a model wind farm where the turbines were represented by perforated disks, while Bossuyt et al.[35] used 100 PDs to measure the spatiotemporal power output from wind farms in different arrangements.

While PDs have already been used as static wind turbine models, several studies also focus directly on the flow field around them. Early PD experiments were performed by Sforza et al.[36] They measured the wake expansion and velocity deficit downstream of perforated disks with different solidity. Instead of using perforated disks, Cannon et al.[37] used wire mesh disks in their flow visualization of the wake downstream of disks with different solidity. For disks with a solidity lower than 60%, they did not observe vortex shedding in the wake, in contrast to the vortex shedding seen behind solid disks (SDs) and wire mesh disks with higher solidity. The near wake of slotted disks of different solidity was investigated by Higuchi et al.[38] They reported that the three-dimensional structures downstream of the perforated disks are more axisymmetric than those behind a solid disk. More recently, Myers and Bahaj[39] showed that beyond 6D downstream of wire mesh disks, the wake velocity deficit is nearly independent of the disk solidity when it is varied. Lin et al.[40] found that the wake of a perforated disk with a solidity of 88% had a higher maximum velocity deficit than the wake of a solid disk in the range from 3D to 5D downstream, and that the structure of the recirculation zone was different between the disks. This is in contrast to results reported by Xiao et al.,[41] which reported lower velocity deficit in the wake of a perforated disk with 75% blockage compared to the wake of a solid disk. Ranjbar et al.[42] investigated the drag, induction factor, and the power coefficient estimated from the induction factor for porous disks of different solidities. Recently, Huang et al.[43] introduced a new scaling parameter $D^* = 4A/P$, with A being the disk area and P the perimeter, to match the wake recovery of porous disks of different geometries: circular, square, and rectangular.

Several studies have assessed the feasibility of using ADs as wind turbine models in simulations, both for single turbines (e.g., Ref. 44) and for several interacting turbines (e.g., Ref. 45). To validate the usage of PDs in wind tunnel experiments, Aubrun et al.[46] performed hot-wire measurements in the near wake of a rotating turbine and a wire mesh disk. They found reasonable agreement up to the fourth-order turbulence statistics in the wake 3D downstream of the wake generating objects (WGOs), both in decaying isotropic turbulence and in an atmospheric boundary layer. Later, Lignarolo et al.[47] used stereo particle image velocimetry (SPIV) to capture the near wake of a wire mesh disk and a rotating turbine. They showed that the wakes agree well, but that the TI is higher in the shear layer of the turbine than the disk. It was also shown that the total flux of kinetic energy into the wake is equal for the two cases, although the tip vortices from the turbine contribute both with a positive and a negative flux, meaning that the transport mechanisms are different in the different wakes.[47] The difference in the instantaneous structures of a PD wake and a rotating turbine wake was recently emphasized by Helvig et al.[12] They showed that the coherent structures in the near wake differ both in size and location between a rotating model and a porous disk. Neunaber[48] has later confirmed that the PD and wind turbine wakes mix differently in the near wake, but that the centerline evolution in the far wakes is similar.[49] These studies did not use a wire mesh disk, but they have a design with nonuniform blockage and without an outer solid rim. Similar disks, but with a solid circumference, were used by Camp and

Cal.[50,51] They used a 3 × 4 array of turbines and disks, and did particle image velocimetry (PIV) around the center turbine in the last row. In the far wake, the mean kinetic energy transport is captured well by the PD. However, they highlight the importance of properly choosing the design of the PD. The near wake features of PDs were examined by Theunissen and Worboys.[52] They varied the hole topology and positions of high solidity PDs and observed near wake features as for example jet mixing.

The aforementioned comparisons generally target the near wake, with limited information downstream of approximately 5D from the WGO. This is upstream of where subsequent turbines are placed in several real wind farms (Table I). Furthermore, there is no agreement on what is the best design philosophy for such PD models. Aubrun et al.[53] began to address this by comparing the wakes of two actuator disks in different facilities at 4D. Later, Helvig et al.[12] compared several PDs to a rotating model, detailing how one of the disks generated a wake more similar to the wake of a rotating model. Although the results showed good agreement in the mean features, their analysis showed discrepancies between the wakes with regard to the temporal structures in the flow, and again the results were limited to the near wake, stopping at 3.5D.

This work fills a knowledge gap by performing measurements in the wakes of two different PDs and a power extracting wind turbine model at distances up to 30D downstream. Such measurements are important in that wake modeling essentially assumes an asymptotic self-similar state, which in turbulence is rarely assumed to begin within the first tens of characteristic lengths from a body; but, this is the exact region of interest in wind energy. There is thus a need to investigate if wakes of different PDs with the same drag and at the same characteristic velocity in fact do approach one another before the typical position of the next turbine; and if not, do they ever agree within the measurable range of the experimental facility? The measurements were performed in low-turbulence, uniform conditions, rather than in a turbulent boundary layer, to isolate the effect of changing the geometry of the WGOs. The design of the two PDs is different in their nature: whereas one of them is a wire mesh, the other is a perforated disk with nonhomogeneous blockage. As a reference case, the wake behind a solid disk was also measured. Turbulence statistics from first- to fourth-order velocity moments are presented. This is thus the first study evaluating the ability of PDs to replicate a wind turbine far wake. It also presents a first glance at a detailed comparison of the far wake downstream of different PDs used as wind turbine models.

II. EXPERIMENTAL SETUP

A. Disks and wind turbine

The two ADs used in the present study have a diameter of $D = 200$ mm and a solidity of $\sigma = 57\%$. The solidity is thus lower than the limit of where vortex shedding was observed by Cannon et al.[37] The first disk was cut from an industrially manufactured wire mesh with a wire thickness of 0.8 mm, and has a uniform blockage. The disk, here referred to as the uniform disk (UD), is the same as the uniform PD used by Aubrun et al.[53] in their blind test comparison. The other disk was designed to have the same solidity as the UD but now with a nonuniform blockage. It is therefore referred to as the nonuniform disk (ND). The ND has ribs expanding from the center to a solid rim. The blockage is highest near the center of the disk, which replicates the relatively large size of the wind turbine blades at the same location and the nacelle. The design is based on the nonuniform disk used by Aubrun et al.[53] and Camp and Cal.[50,51] The ND was machined from a 5 mm thick acrylic sheet to match the diameter and solidity of the UD. Schematics of the UD and ND are shown in Fig. 1. The drag of the disks was measured using a force balance, and it was found that $C_D = 0.77$ and $C_D = 0.82$ for the UD and the ND, respectively. As a reference case, the wake of a wooden, 9 mm thick, solid disk (SD) with the same diameter, $D = 200$ mm was also measured. The SD has $C_D = 1.1$, as expected for this geometry. All the disks
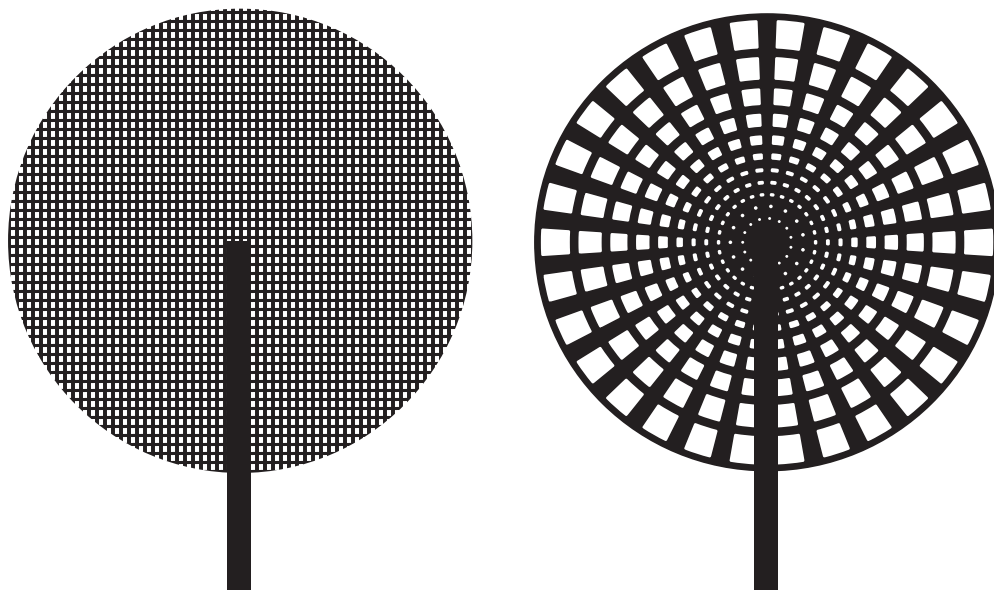

FIG. 1. Schematics of the uniform disk, UD, (left) and the non-uniform disk, ND, (right) mounted to towers.

were attached to a 10 mm diameter steel rod, which in turn was mounted to a thicker steel rod with a diameter of 32 mm. The thicker mast stops 200 mm below the hub height. To reduce the influence of the thicker rod, a cable was wound around it to act as a vortex disruptor.[54] The length of the rods was adjusted in order for the disks to be located in the vertical and horizontal center of the wind tunnel cross section such that the wake is not affected by the boundary layers of the wind tunnel walls.

The wind turbine (WT) is a three-bladed, speed-controlled fixed-pitch turbine. It has the same diameter as the disks, $D = 200$ mm. The blades were 3D-printed with a stereolithography printer, with the NACA 63–418 airfoil profile along the entire blade. The chord of the blade ranges from 25 mm at the hub to 12.5 mm at the tip, and the geometrical pitch angle ranges from $\theta = 39.57°$ to $\theta = 0.73°$. The values were chosen to give a constant angle-of-attack (α) of $12°$ along the blade at a tip speed ratio $\lambda = 3.5$, which yields good turbine performance according to blade element momentum simulations. The hub of the turbine has a diameter of 22 mm, and the generator, encoder, and wiring were enclosed in the nacelle, which has a diameter of 24 mm and was 3D-printed with a filament-deposit printer using poly-lactic acid (PLA). Furthermore, the nacelle was mounted to a rod with a diameter of 20 mm. This rod was mounted to the same mast as the actuator disks. Figure 2 shows the WT mounted in the wind tunnel.

The rotational speed of the WT was set to achieve the maximum power coefficient, C_p, at the given incoming velocity. Figure 3 shows the power curve of the WT, with the dotted vertical line illustrating the operating point at $\lambda = 3.65$, which is close to the λ that was used to determine the geometrical pitch of the blade. Details about the control and electronics of the WT can be found in a recent paper by Gambuzza and Ganapathisubramani.[55] They use the same control system on a slightly smaller turbine. Due to constraints in the experimental setup, it was not possible to measure the drag of the rotating turbine. Through wake integration, the drag of the WT was found to be smaller than the drag of the PDs, although this method is not
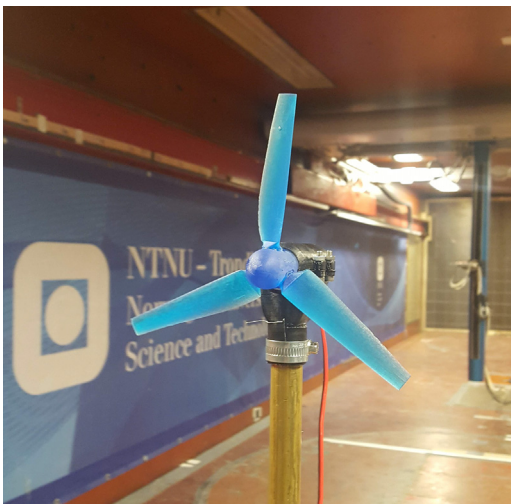

FIG. 2. The wind turbine model, WT, mounted in the wind tunnel. The traversing system with the hot wires can be seen in the background.
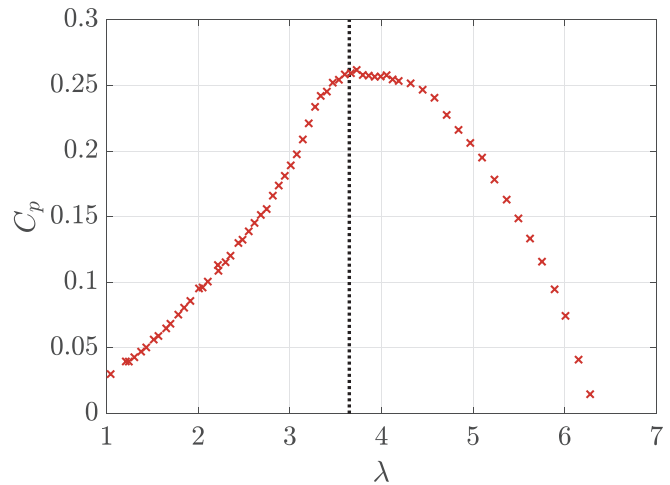

FIG. 3. C_p at different λ. In the experiments, $\lambda = 3.65$ illustrated by the dotted line, was used.

robust enough to yield exact values due to the 3D nature of the flow. Nevertheless, important features, such as tip vortices and rotation of the flow, are present in the model WT wake. The main focus of this work is on the disks, and thus the turbine is only used for qualitative comparison of the flow features given the disparity in drag.

B. Facility

The experiments were performed in the $11.15 \times 2.71 \times 1.80$ m³ (length × width × height) closed loop wind tunnel at the Norwegian University of Science and Technology. The height of the roof was gradually increased from 1.80 m at the inlet to 1.85 m at the outlet of the test section to compensate for the growing boundary layer thickness. The WGOs cover an area well below 1% of the wind tunnel cross section, and blockage effects are negligible. To ensure low TI and homogeneous flow, a wire mesh screen was installed at the inlet of the test section. The WGOs were mounted 1.6 m downstream of the contraction, corresponding to 640 mesh lengths (M) downstream of the screen. A schematic of the facility is shown in Fig. 4.

Hot-wire anemometry (HWA) was used for all velocity measurements. Three Dantec Dynamics 55P11 single-wire probes, operated in constant temperature mode, were used for simultaneous sampling. They were connected to a Dantec Dynamics StreamLine Pro anemometer. The sampling frequency was 30 kHz, with an analog low-pass filter applied at 10 kHz. An automated traversing system was used to make horizontal scans at six different downstream locations, $x/D = 3, 5, 10, 15, 20,$ and 30, illustrated by ×-symbols in Fig. 4. All scans were performed at hub height. It should be noted that the hub height does not represent the wake centerline, as the tower shifts the wake downward.[56] However, in many wind farms, the turbine hubs will be at the same height; thus, hub-height measurements are of utmost important for any downstream turbine. At the beginning and end of each day of the campaign, the probes were calibrated against a pitot-tube. The temperature was recorded with a thermocouple, and the calibrations were corrected for temperature variations according to the procedure outlined by Hultmark and Smits.[57] A weighted average,
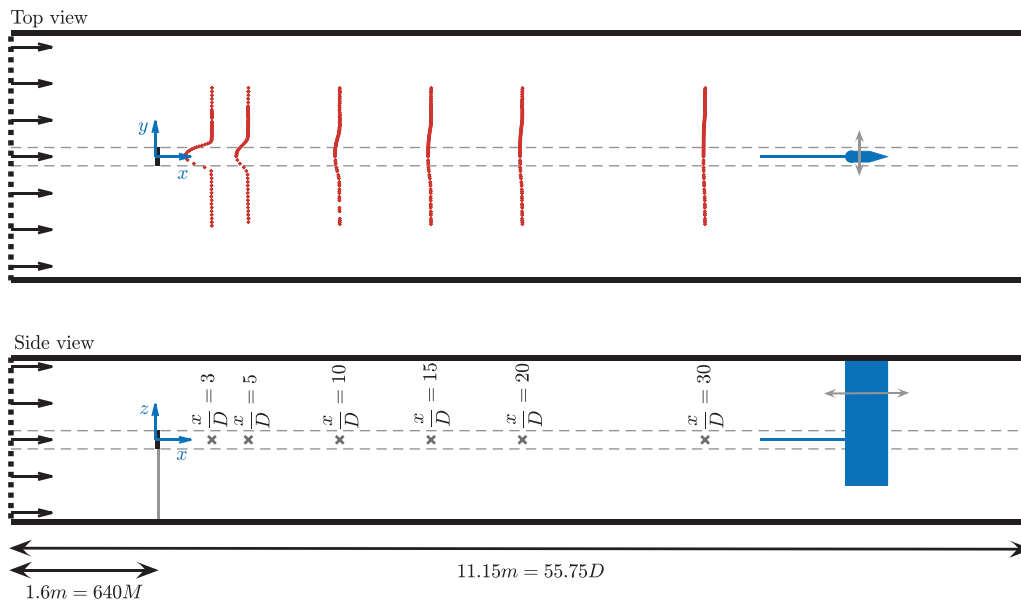
FIG. 4. Schematics of experimental setup in the test section of the wind tunnel. The streamwise locations of the hot-wire scans are marked with $\times$ in the side view. The velocity profiles for the non-uniform disk are shown in the top view.

based on the time between acquisition and each of the two calibrations, was used to convert the voltage signal to velocity.

In the wake of the WT, the distance between each measurement point in the scan was 10 mm at all downstream positions. In the wakes of the disks, which are expected to be symmetric, only half the wake was scanned with 10 mm distance between the measurement points. To check for symmetry, the other half of the wake was scanned with a maximum distance between two measurement points of 50 mm. In the freestream, outside of the wake, the larger distance was used. To ensure good convergence of turbulence statistics up to the fourth order, 360 s measurements were taken when the distance between the measurement points was small. For the lower density measurements, 200 s samples were used. The measurements from the three different wires were normalized to each other by the first measurement in each profile scan. To account for hot-wire drift, the last measurement was normalized to the first measurement for the separate wires. All the normalizing measurements were taken well outside the wake region. For the profiles farthest downstream of the SD, the wake outgrew the traverse limits such that normalization was not possible. Instead, correction factors for the start and end of each scan were found by minimizing the least squares error between the separate wire profiles. A weighted average of the correction factors was used across the scans. This procedure was only applied at the two most downstream profiles and only influences the mean velocity profiles, not the higher-order statistics.

The velocity and turbulence profiles of the background flow were measured with hot-wire anemometry at six different streamwise positions. The incoming velocity was $U_\infty \simeq 8.1$ m/s, corresponding to a Reynolds number of $Re = (DU_\infty)/\nu \simeq 10^5$. At each position, a 200 s sample was taken. The profiles are shown in Fig. 5. The velocity is uniform within $\pm 1\%$ for all streamwise positions. Recall, the WGOs are located in the center of the tunnel, far away from the boundary layers

of the tunnel walls. A small shear is observed in the center of the tunnel, with the velocity on the positive side ($y > 0$) being slightly higher. This small shear shifts the wakes of the WGOs slightly toward $y > 0$. For all the WGOs, at all downstream positions, this shift is within 2% of the distance from the object. The shift is also approximately the same for the different objects. Based on this, the small velocity gradient was judged to be acceptable. The TI, defined as u'/U, where U is the local mean velocity and u' is the standard deviation of the velocity fluctuations, is also shown. The values are below 6×10^{-3} across the tunnel (0.6% turbulence intensity). The small shear in the tunnel leads to a peak and asymmetry in the TI profiles. The other parts of the
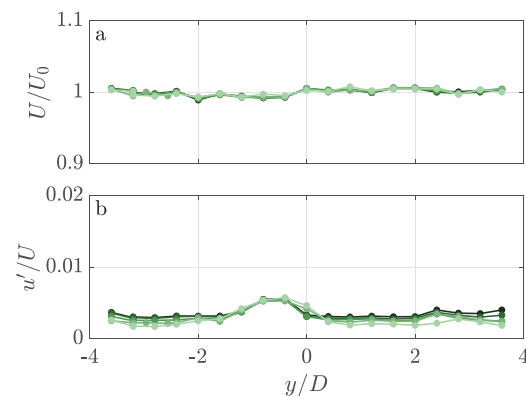
FIG. 5. Mean velocity (a) and turbulence intensity, TI, (b) of the background flow in the wind tunnel. The velocity is normalized by the mean velocity across the tunnel, U_0. Measurements are taken at five streamwise positions – $x = 0D$, $0.5D$, $3D$, $10D$ and, $30D$ – at the height of the center of the wake-generating objects. The colors in the figure range from dark at $0D$ to light at $30D$.
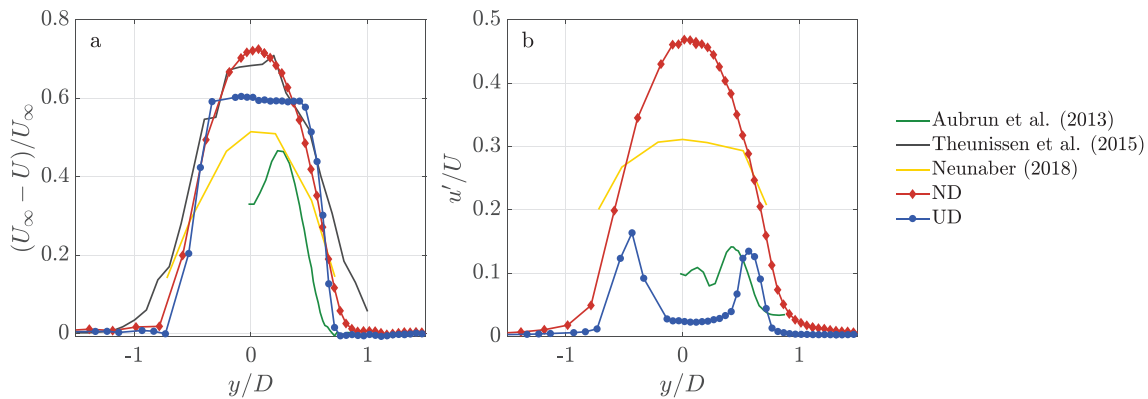
FIG. 6. Velocity deficit (a) and turbulence intensity, TI, (b) of disk wakes from the present study and the literature. The profiles are taken at positions close to $x = 3D$.

profiles have values around 3×10^{-3} (0.3% turbulence intensity), decaying with increasing downstream distance. Overall, these values are quite low for a facility of this size.

III. BASELINE COMPARISON TO OTHER STUDIES

Wind turbine and PD wakes have been reported extensively in the literature (e.g., Refs. 4, 34, 46, 48, 58, and 59). To put the current results into context, the velocity deficit ($(U_\infty - U)/U_\infty$) and TI measured in the present study are compared to a sample of results from existing studies that could be accessed. The comparison is made at $x \approx 3D$, as this is a common measured position for most studies. In Fig. 6, the velocity deficit and the TI in the wake of several PDs are shown. The different studies used in the comparison are briefly summarized in Table II. The velocity and TI profiles differ between the studies. Some of the discrepancies are due to the different C_D of the disks; also, the shape of the profiles is different between the disks. The velocity deficit ranged from rounded, Gaussian-like profiles to top-hat profiles, with the ND and the UD representing the two extremities, respectively. Large discrepancies in the TI profiles can also be observed between the disks. In total, the wake of the ND is somewhat similar to the wake of Neunaber's[48] disk, while the wakes of Aubrun's[46] disk and the UD show some similarities in the TI profiles. To improve wind turbine models, it is important to understand the physics leading to these differences. To that measure, the two different PDs used in this work are reasonable design choices, as the shape of their velocity deficit and TI profiles differ from each other and cover the span of differences seen between earlier disks.

Similarly, the wake of the rotating model has been compared to different earlier wake measurements, ranging from lab-scale to full-scale measurements. The results are shown in Fig. 7. Information about the presented studies can be found in Table III. Most of the turbines, including the WT used in the present study, have an asymmetric wake. However, the wakes reported by Medici and Alfredsson[4] and Neunaber[48] are close to symmetric. Also here, some of the differences arise from different operating conditions. This effect is particularly evident in the full-scale measurements by Zhan et al.[59] Two of the cases they report are shown in Fig. 7. While these are wake measurements of the same turbine, the different operating conditions during the measurements change the wake. Clearly, it is difficult to compare PD models to rotating models and full-scale wind turbines when even the benchmark is highly dependent on operating conditions.

Nonetheless, the figure shows that the WT used in the present study has a wake that, with respect to the magnitude of the velocity deficit and TI, and the width of the wake, lies within typical results from other studies. Only the full-scale measurements by Zhan et al.[59] show wider wakes, but the results they present are obtained by averaging velocity measurements over a small range of different incoming conditions and wind directions over a fixed time, which could possibly make the wake appear wider. In addition, the shape of the WT wake profile qualitatively agrees well with the full-scale measurements by Zhan et al.[59] despite the lower C_D. Thus, the WT is a suitable benchmark for the present investigation where we can rigorously control the experimental conditions.

IV. RESULTS

A. Mean velocity and turbulence intensity

A wind turbine's power production is governed by the incoming velocity. It is therefore important to match the wake velocity profile of

TABLE II. List of actuator disks in Fig. 6.

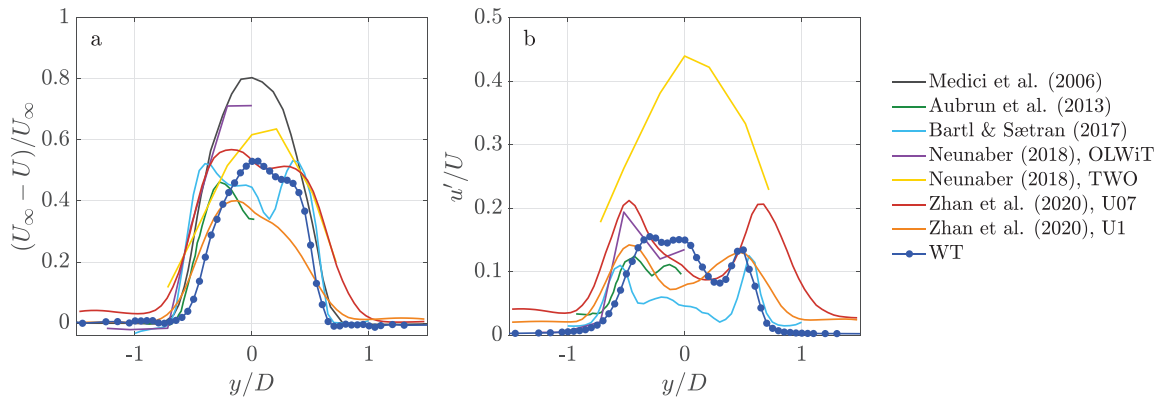| Reference	Description	Re	x/D	C_D	Solidity	Technique
Aubrun et al. (2013)[46]	Wire mesh	7×10^4	3		0.45/0.35	HWA, 1C
Theunissen et al. (2015)[34]	Holes	4×10^4	3		0.86	LDV, 2C
Neunaber (2018)[48]	Ribs	3×10^5	2.97	0.96	0.53	HWA, 1C
ND	Ribs	1×10^5	3	0.82	0.57	HWA, 1C
UD	Wire mesh	1×10^5	3	0.77	0.57	HWA, 1C

FIG. 7. Velocity deficit (a) and turbulence intensity, TI, (b) of turbine wakes from the present study and the literature. The profiles are taken at positions close to $x = 3D$.

a PD's wake to a wind turbine wake. Figure 8 shows the velocity deficit of all WGOs used in this study. All six downstream positions are presented in the different subfigures.

The SD and the ND both have rounded velocity profiles at $x = 3D$. The maximum velocity deficit is high for the ND this close to the disk. For both the mentioned disks, the velocity deficit diminishes rapidly farther downstream. At the same time, the wake extends horizontally, spanning the entire range of the measurements at $x = 30D$. The SD wake is wider than the ND wake, throughout the measurement region, but it has a lower maximum velocity deficit. This is in agreement with Lin et al.[40] but in contrast to Xiao et al.[41]

In the near wake, at $x = 3D$, the UD generates a different wake. The velocity deficit has a top hat profile, with strong velocity gradients at the edges of the wake. The UD reduces the velocity evenly across its cross section. From $x = 5D$, the velocity gradients are reduced. However, the maximum velocity deficit increases slightly between $3D$ and $5D$ downstream of the disk. The maximum velocity deficit is reduced farther downstream, but not as much as for the ND. For $x \geq 5D$, the disk has the highest maximum velocity deficit of all the WGOs. The wake is also smaller in width, keeping the high velocity deficit in the center of the wake, in contrast to the velocity deficit in the ND wake, which is spread out over a larger area. Hence, there are large differences between the wakes of the two PDs, even though they are generated by disks with the same diameter, solidity, and approximately the same C_D. Note that here, the normalized velocity deficit is

plotted, such that both shape and magnitude could be evaluated. In Appendix A, figures of the self-normalized velocity deficit and TI are provided, to allow for better comparison of the shape of the wake profiles. The self-normalized profiles further indicate that the shape of the mean velocity profile that best matches the WT is the UD, at least for $x/D \geq 10$.

The WT wake has a smaller velocity deficit than the ND and UD at $x = 3D$, which is related to its lower C_D. As such, we offer the comparison to this model in order to identify phenomenological features of the WT wake and its general shape, rather than a direct comparison to the velocity deficit. The WT wake is asymmetric, as was also seen in Fig. 7. The reduction of the maximum velocity deficit is slower compared to the ND, and already at $5D$ downstream, the maximum velocity deficit is higher for the WT despite the lower C_D. The expansion of the wake width is also smaller. Figure 9 shows both the evolution of the wake width and the evolution of the maximum velocity deficit for all WGOs. The wake width, $\Delta\delta_{0.5}$, is defined as the distance between the two points where the velocity deficit is half the maximum velocity deficit, and is displayed in Fig. 9(a). The expansion of the wake of the WT and the UD collapses very well for $x \geq 10D$, while the SD and ND grow much faster. It is interesting to note that the latter two grow at approximately the same rate, even though their width is different. The evolution of the maximum velocity deficit, displayed in Fig. 9(b), does not show the same behavior. Still, the decay of the maximum velocity deficit is more rapid in the ND wake than the WT and UD

TABLE III. List of turbines in Fig. 7.

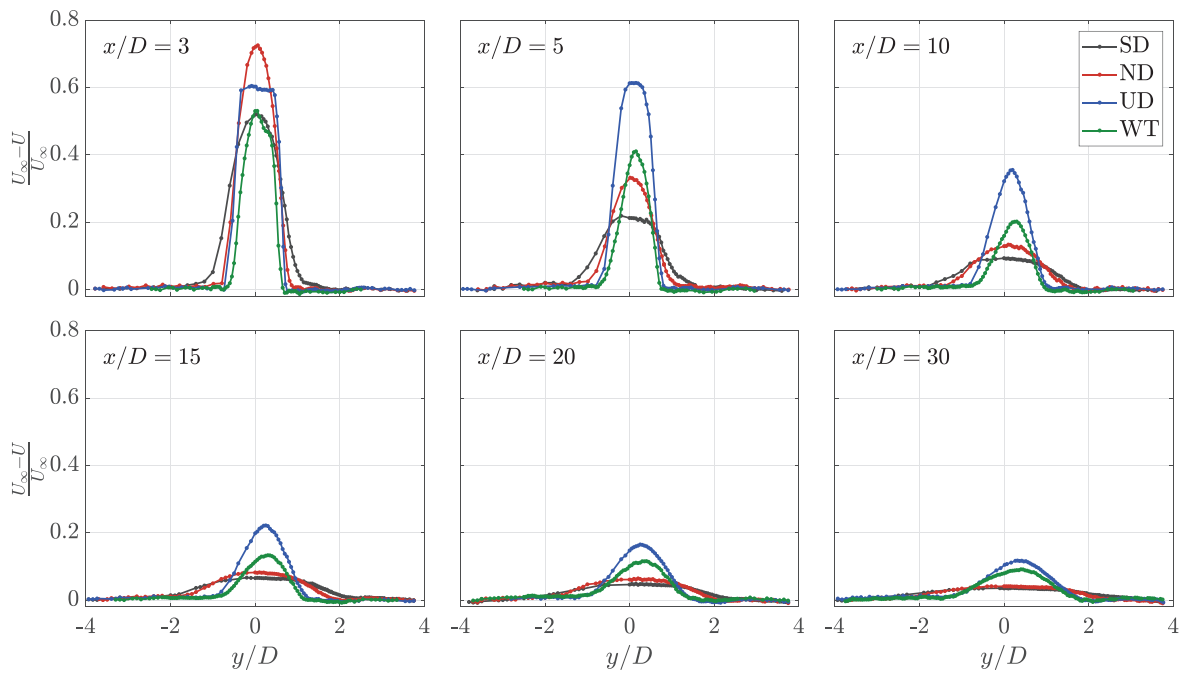| Reference	Re	x/D	No. blades	C_D	λ	Technique
Medici and Alfredsson (2006)[4]	1×10^5	3	2	0.794	3.66	HWA, 2C
Aubrun et al. (2013)[46]	7×10^4	3	3	0.5	5.8	HWA, 1C
Neunaber, TWO (2018)[48]	3×10^5	2.97	3	1	5.7	HWA, 1C
Neunaber, OLWiT (2018)[48]	3×10^5	2.97	3	1	6.2	HWA, 1C
Bartl and Sætran (2017)[58]	7×10^5	2.77	3	0.811	6.0	HWA, 1C
Zhan et al. (2020)[59]	Full-scale	2.75	3			LiDAR
Zhan et al. (2020)[59]	Full-scale	2.75	3			LiDAR
WT	1×10^5	3	3		3.65	HWA, 1C

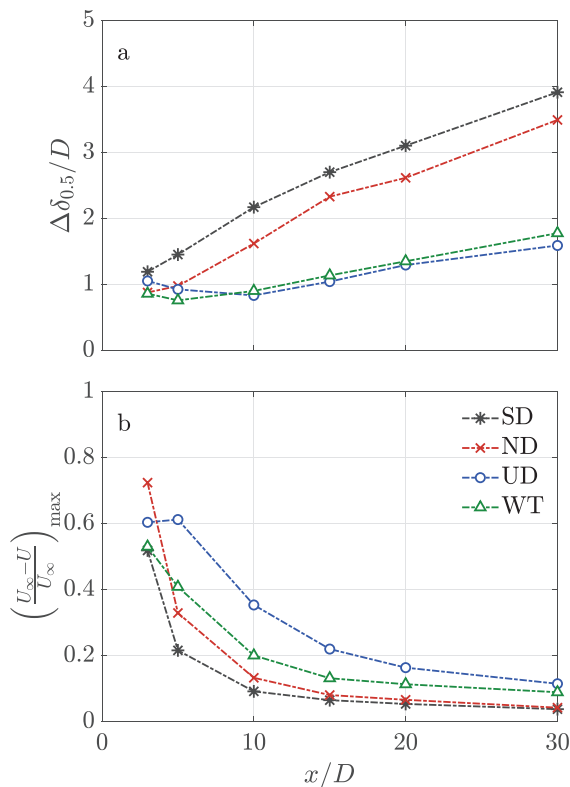**FIG. 8.** Velocity deficit profiles at all downstream positions.

FIG. 9. Evolution of the wake width (a) and velocity deficit (b) at different positions downstream of the wake-generating objects.

wakes. One reason for the discrepancy between the UD wake and WT wake could be the difference in C_D. No comparison to analytical wake models or axisymmetric wake theory has been included in this work. The downward shift of the wake, due to the tower,[56] makes it unfeasible to compare it with a general axisymmetric wake.

The TI profiles of the wakes are shown in Fig. 10. In the center of the SD and ND wakes, at $x = 3D$, the TI is at a level where hot-wires cannot accurately measure it due to backflow events.[60] These magnitudes should therefore be considered with caution. The high turbulence levels enhance the transport of momentum from the freestream into the wake. This explains the rapid wake expansion and reduction of the velocity deficit for the SD and ND, as was shown in Figs. 8 and 9.

On the other hand, the turbulence levels close to the UD are lower, but also decrease much slower. At $x = 3D$, the highest levels of turbulence are found at the edge of the wake, where the velocity gradient is high. In contrast to the SD and ND wakes, the TI is low in the center of the wake. Until $x = 10D$, the maximum TI in the wake stays around the same magnitude, but the peaks located in the shear layer grow in width and at $x = 10D$ they have merged to span the entire wake. Farther downstream, the turbulence decays, although the levels stay higher than for the SD and the ND wakes also for $x > 10D$.

The two PD designs produce wakes with different characteristics, even in the low order statistics. The ND produces several jets of different sizes, as can be seen in the PIV fields in the work by Helvig et al.[12] and Thenuissen and Worboys,[52] where the former used disks with very similar design to the ND. The high local velocity gradients in the wake produce turbulent energy; thus, the TI is increased. The high levels of TI increase transport, which spreads the wake and reduces the maximum velocity deficit. The UD has a fine mesh, such that the majority of turbulent production arises in the high shear regions in
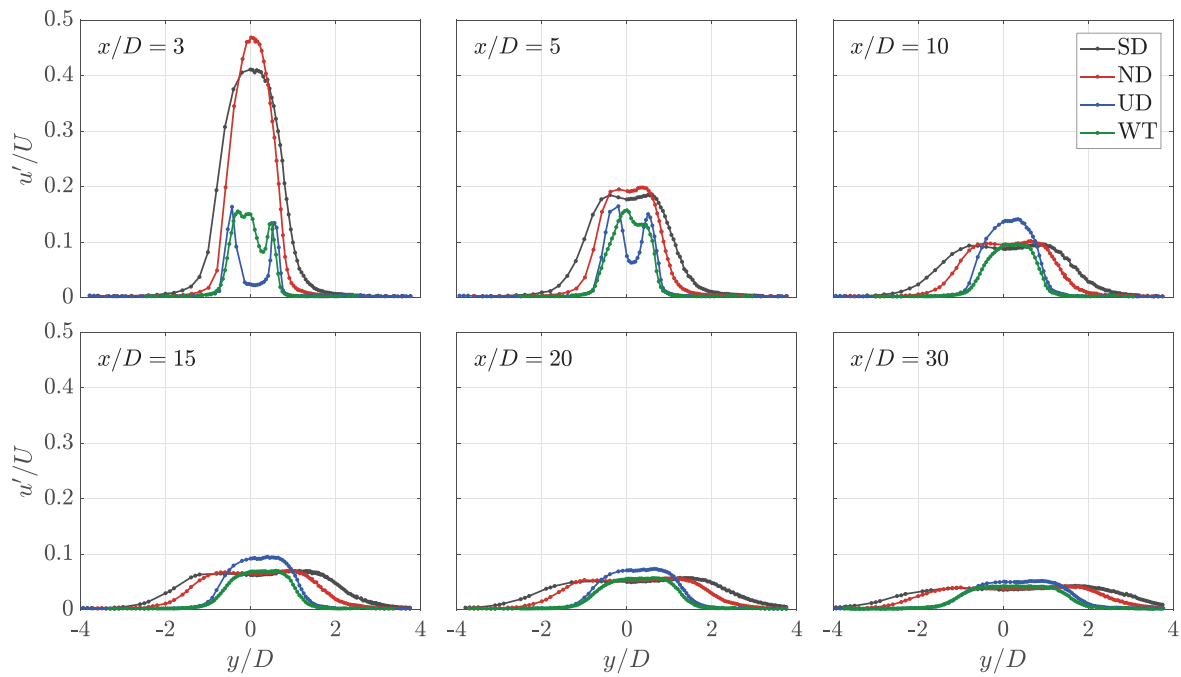
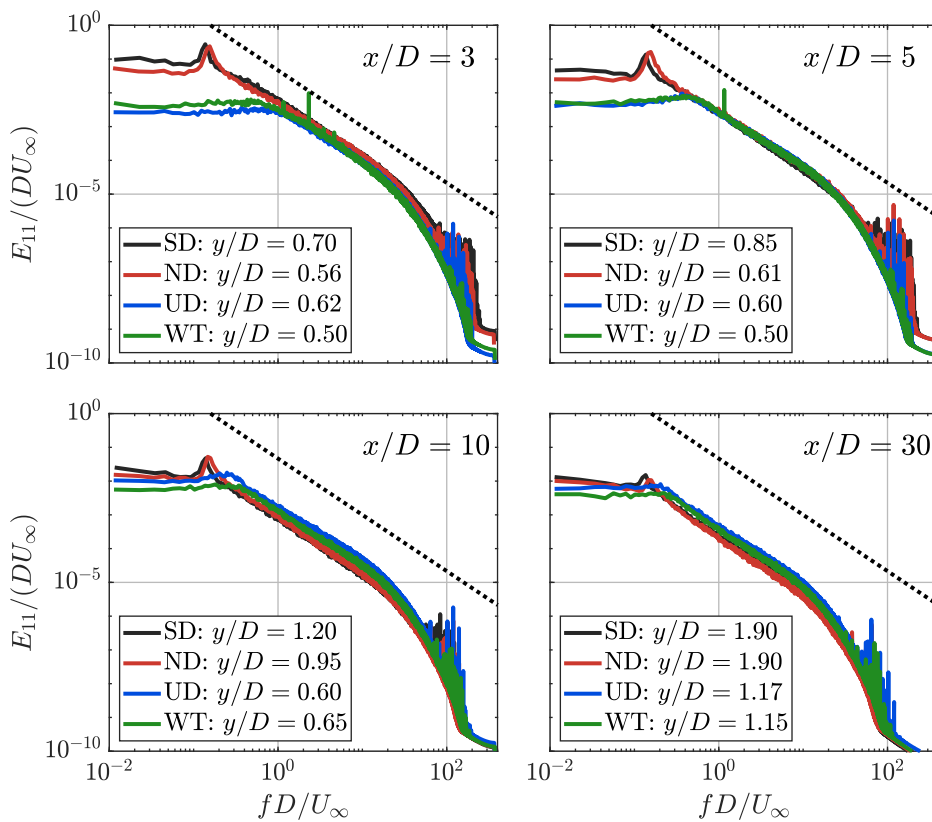**FIG. 10.** Turbulence intensity profiles at all downstream positions.

FIG. 11. Velocity spectra at different downstream positions. All spectra are taken at the position where the velocity deficit is closest to half the maximum velocity deficit, i.e., in the shear layer.

the wake. As the high levels of shear extend farther downstream from the disk, production continues farther downstream, maintaining higher levels of turbulence in the far wake.

For the two closest positions, the WT wake has an asymmetric TI profile. This arises from combined effects of the tower wake and the rotation of the turbine wake, and has been reported earlier.[61] At these two positions, the levels of TI are close to the ones in the UD wake. However, the TI is higher than for the UD in the center of the wake. The turbulence also decays more rapidly in the WT wake from $x = 5D$. Figure 8 shows that the velocity gradients in the WT wake are smaller than for the UD, but larger than the wakes behind the other WGOs. The TI profiles demonstrate that the disks are unable to replicate the TI profile in the WT-wake, although the UD does lead to comparable magnitudes of TI, and the wake widths are approximately the same for the two. It should be noted that Helvig et al.[12] recently showed that even though the mean profiles of wind turbine and porous disk wakes show reasonable agreement, the instantaneous structures might differ significantly.

B. Velocity spectra

The first- and second-order statistics give valuable insight into the mean wake features. However, they do not give information about the structures in the wake. Such structures are important for loads on downstream turbines.[2] To obtain information about the structure of the wake, the power spectral density of the velocity fluctuations (E_{11}), here referred to as the velocity spectrum, of the wakes was studied. Some selected spectra are shown in Fig. 11. The spectral comparisons have been made at the measurement positions where the velocity deficit is closest to half the maximum velocity deficit in each wake; this is within the shear layer for each flow. By evaluating in the shear layer rather than at the same physical position in each wake, different flow features at the same relative position in the wake can be assessed. For reference, the same comparisons made at the same physical location are presented in Appendix B.

There are distinct low frequency peaks in the velocity spectra for the SD and the ND, which are present all the way to $x = 30D$. The Strouhal numbers, $St = fD/U_\infty$, of the peaks are $St = 0.137$ and $St = 0.150$, respectively, for the two disks. The former corresponds to the expected St of vortex shedding downstream of a circular disk (e.g., Refs. 37, 62, and 63). As the latter is only slightly higher, it is also believed to be the standard vortex shedding for an ND. No distinct peaks are observed in the UD spectra, and there is thus no strong vortex shedding in this wake. This is in agreement with the results reported by Cannon et al.,[37] who did not observe vortex shedding in the wake of wire mesh disks when the solidity was less than 60%.

At the closest measurement position, three sharp peaks are observed in the WT spectrum. The first peak has a reduced frequency of $St = 1.159$, which is the rotational frequency of the WT. The two other peaks are at reduced frequencies of 2.320 and 4.640, and are thus harmonics of this first one. For the WT, there is no strong periodic energy associated with vortex shedding for most of the wake, which differs from that present behind SD and ND.

To illustrate the extent of the vortex shedding, spectrograms of different cases have been prepared. A spectrogram is a collection of spectra plotted beside each other, with a colormap indicating the magnitude of energy at the different frequencies. An example spectrogram is shown in Fig. 12(a). The vertical axis shows the frequency,
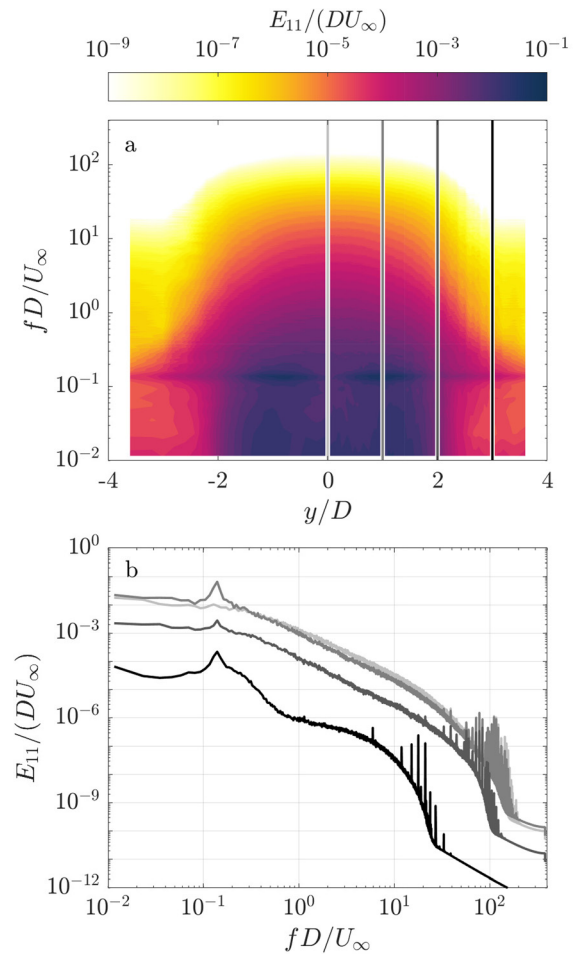
FIG. 12. A graphical explanation of spectrograms. (a) Spectrogram of the SD wake at $x = 10D$. (b) Four spectra plotted in the traditional way, corresponding to the vertical lines in panel (a).

corresponding to the x axis in a conventional plot of a spectrum, while the horizontal axis shows the y-position in the wake. In that sense, each vertical line in Fig. 12(a) is a spectrum, shown in Fig. 12(b) with the respective color. The colormap displays the energy content, thus representing the y axis in a typical spectrum. The spectrograms allow investigation of the spanwise extent of structures in the flow, as well as a direct comparison between the same physical position in the different wakes.

Figure 13 shows spectrograms at representative downstream positions. The velocity spectra integrate to the variance of the velocity, equivalent to the square of the turbulence intensity when the mean velocity is held constant across test cases as done here. Thus, the color intensity of the spectrogram agrees with the TI profiles in Fig. 10. The vortex shedding associated peaks are visible for the SD and ND, highlighted with (i) in the figure, spreading over the entire width of the wake and also some distance outside the high-energy regions. Even 30D downstream of the disks, traces of vortex shedding can be seen for both disks. As discussed in relation to Fig. 11, no such vortex
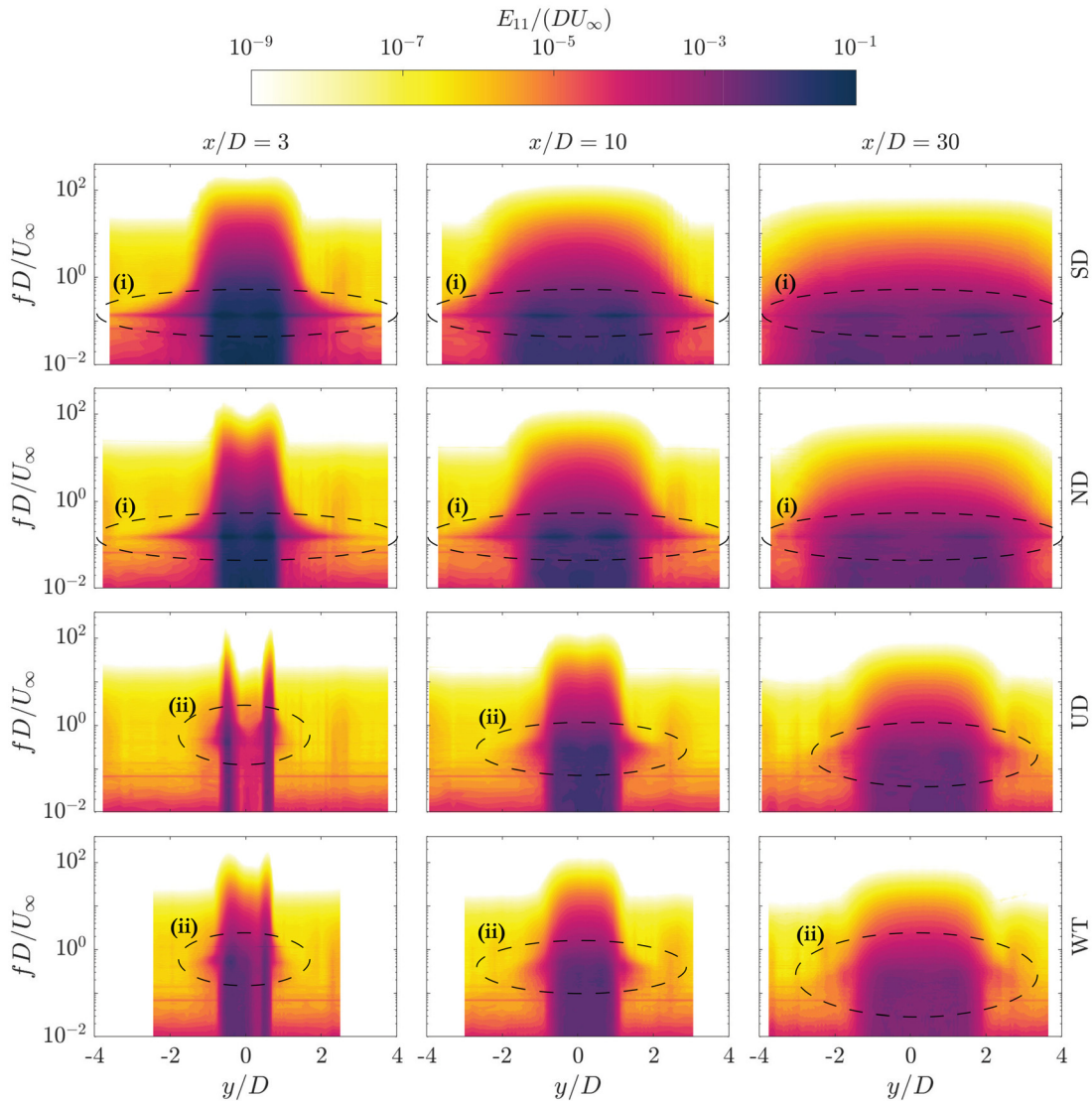
FIG. 13. Spectrograms at representative downstream positions. The dashed ellipses highlight vortex shedding frequencies (i) and instantaneous structures arising from the strong shear (ii).

shedding peak is observed for the UD and WT wakes. However, at the edges of the high-energy regions, a range of energy containing frequencies are present, marked with (ii) in Fig. 13. These frequencies are higher than the vortex shedding frequency. The sharp velocity gradients found here are comparable to mixing layer flows, where coherent structures are known to exist.[64,65] Thus, these high-energy frequencies result from the strong shear in the flow. From this and the results in Sec. IV A, the edges of the wakes downstream of the UD and WT act as mixing layer flows due to the strong shear. The same behavior is not observed for the SD and the ND. An analysis of the spectra reveals that different physical mechanisms govern the different wakes. In particular, it is interesting to observe that the ND leads to vortex shedding in the wake, which is not present in the UD wake. In turn,

the UD wake has high-energy structures in the shear layers, although with smaller magnitude than vortex shedding.

C. Velocity skewness and kurtosis

For the structural loads on downstream turbines, it is important to understand the distribution of velocities within the turbulent flow. To that measure, the skewness and kurtosis of the velocity fluctuations can be instructive. Skewness, $\overline{u^3}/\overline{u^2}^{3/2}$, is a measure of the asymmetry of the velocity fluctuation distribution. For negative skew, the extremes of the negative velocity fluctuations are more prominent than the positive ones and vice versa for positive skew. A symmetrical distribution has zero skew.

The skewness of velocity fluctuations at all six measurement positions is shown in Fig. 14. The wakes of both SD and ND have similar skewness profiles throughout the length of the measurements. The magnitude is low in the center of the wake, and the skewness gradually decreases toward a negative peak around the edge of the wake. Then, there is a distinct shift to a positive peak of lower magnitude just outside where the velocity deficit approaches zero. The peak magnitudes are slightly higher for the SD, and as the wake gets wider, they are also farther from the center of the wake.

For the UD, the same inner negative and the outer positive peaks as observed in the SD and ND wake are present, however, with smaller magnitude. In particular, the outermost positive peak is smaller. For $x = 3D$ and $x = 5D$, there are also positive peaks near the center of the wake. Qualitatively, this agrees with the results Aubrun et al.[46] reported for a wire mesh disk at $x = 3D$. A more detailed comparison with those results is not feasible, as their TI (4%) is much higher than the one used in the present work, the solidity of their disk is different, and their disk is not uniform near the center. Farther downstream, the profiles have the same shape as the SD and the ND, but the peaks are smaller in magnitude and are more closely spaced, following from the smaller wake size observed in the lower order velocity statistics.

The fourth-order moment, $\overline{u^4}/\overline{u^2}^2$, referred to as the kurtosis or the flatness of the velocity fluctuation distribution, is another descriptor of the turbulent velocity distribution. The higher the kurtosis, the stronger the tails are. For reference, a Gaussian distribution has a kurtosis of 3 and 0 skewness. If the magnitude of the skewness is large, the kurtosis must also be large, as one of the tails becomes stronger. In Fig. 15, the kurtosis of all the measurement series is shown. There are high levels of kurtosis around the edges of all wakes at all positions.

In turn, this means that the turbulence around the edges of the wake is dominated by extreme events. In the center of the wake, the distribution is close to Gaussian. It should also be noted that the magnitude of kurtosis is higher for the SD and ND than for the UD and WT, showing that extreme velocity deficits happen more often in the wakes of the former disks. It is also worth noting that $3D$ and $5D$ downstream of the UD, there are increased levels of kurtosis in the center of the wake.

There is a clear asymmetry in the skewness and kurtosis profiles of the WT wake at $x = 3D$ and $x = 5D$. The magnitude of both statistics is higher for negative y-values. From $10D$ downstream of the turbine, the asymmetry shifts side, with higher peaks for positive y-values. From this distance, the asymmetry gradually decreases, and the skewness and kurtosis approach the profiles measured in the wake of the UD. This asymmetry is not replicated by any of the disks, but it should not be expected that a static, symmetric disk produces an asymmetric wake. Earlier comparisons of the wake of PDs and wind turbines do not report this asymmetry, but they also only evaluate one side of the wake.[46,47] The interaction between a rotating wake and the wake of the tower is a possible explanation for this asymmetry.

It is noticeable that the magnitudes of both skewness and kurtosis, for all the WGOs, are high at the very edge of the wake, where the TI approaches zero. In this region, bursts of high velocity occur in the flow, increasing the forces acting on downstream turbines. Thus, in agreement with Schottler et al.,[66] the wake is wider than what can be seen in the mean velocity and TI profiles. The turbulence in this outer part of the wake is defined by rare extreme events. For the SD and the ND, these extreme events occur at the very edge of the vortex shedding peak observed in the spectrograms in Fig. 13, and thus have some periodicity. The same periodicity is not present in the edges of the UD and
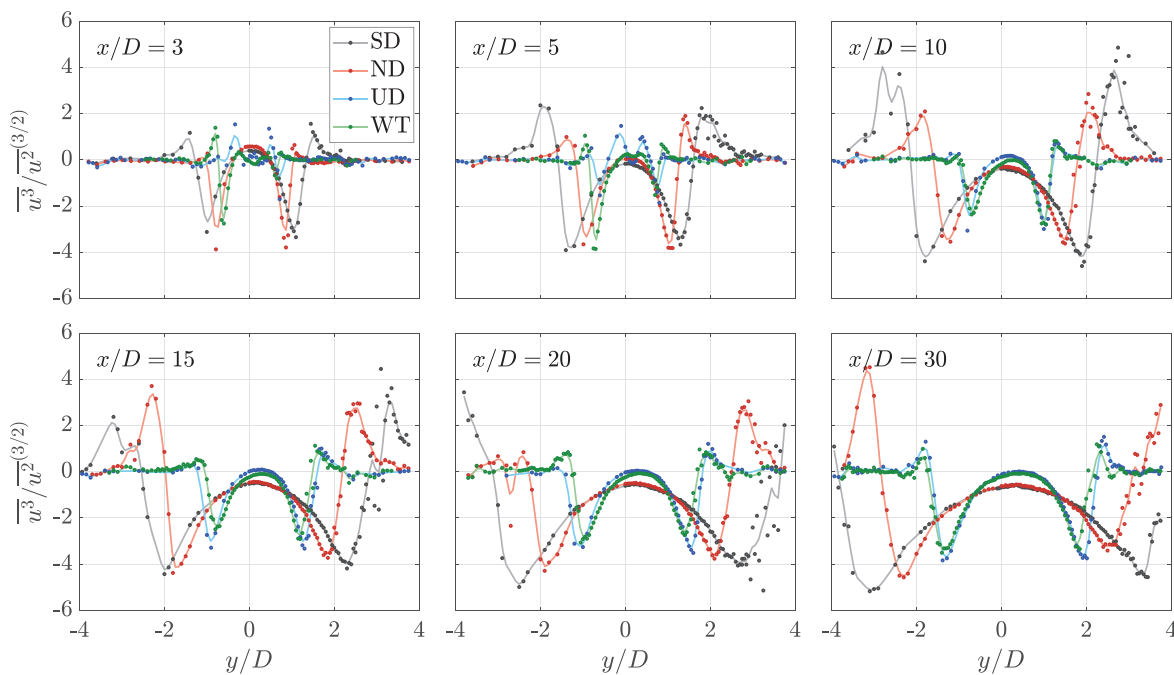

FIG. 14. Profiles of the skewness at all downstream positions. Due to high scatter around the edge of the wake, the solid lines are weighted averages of interpolated data points.
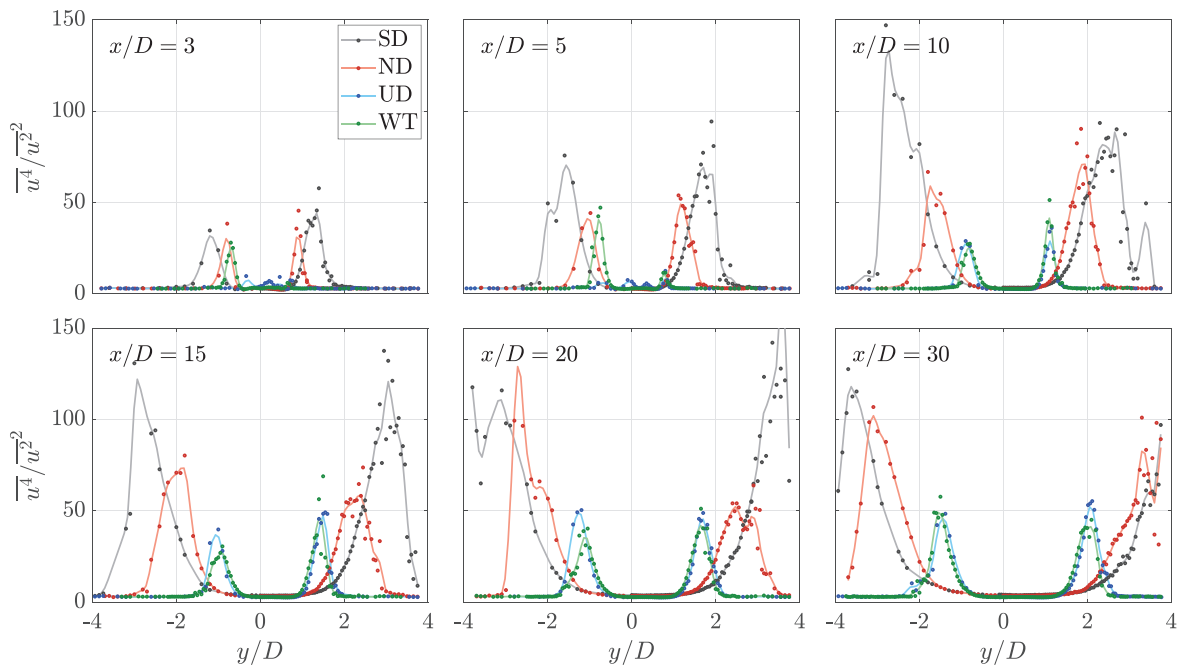
FIG. 15. Profiles of kurtosis at all downstream positions. Due to high scatter around the edge of the wake, the solid lines are weighted averages of interpolated data points.

WT wakes. The lack of vortex shedding might thus be the reason for the lower magnitude of the skewness peaks. In Fig. 16, probability density functions (PDFs) are shown for all WGOs at a streamwise position of $x = 10D$. Both the geometrical centerline and the position of maximum negative skewness are shown. The latter was chosen as a criterion to evaluate a comparable position in the wake of each WGO, instead of choosing a certain y-position in different parts of the wake. At the maximum negative skewness position, the velocity deficit is on the order of 1% or less for all the wakes. The TI is also below 40% of the maximum TI for the respective WGO at the current streamwise position. The geometrical centerline has turbulence levels close to the maximum for each object. The negative tails of the PDF are larger for the position at the edge of the wake than for the centerline position, despite the low velocity deficit and the lower values of TI. Thus, the extreme turbulent bursts have the same magnitude where the velocity deficit approaches zero, as in the center of the wake. The large tails of the PDFs demonstrate that it is important to be able to represent the higher-order turbulent statistics when choosing a wind turbine model. For reference, the PDFs at the same physical locations are presented in Appendix B, but this does not change the findings presented above.

V. CONCLUSIONS

The wakes of two porous disks, one energy extracting wind turbine and a solid disk, have been assessed with hot-wire anemometry. The main focus has been on the differences in the wakes downstream of two different static porous disks and how they replicate the wake of a rotating wind turbine model. The solid disk was included as a
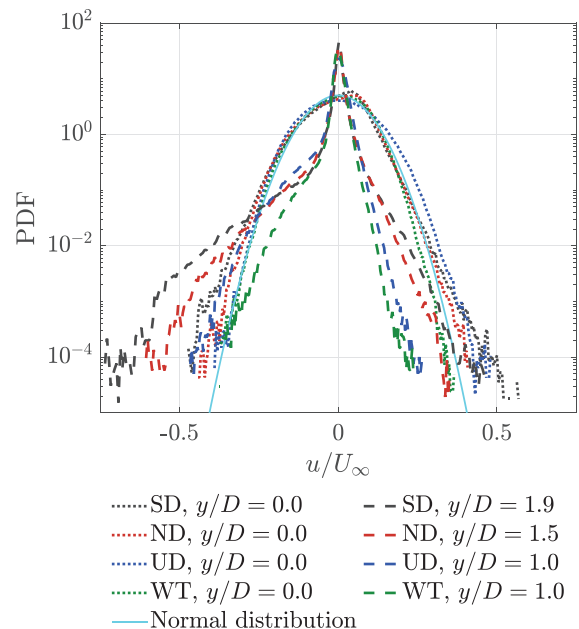

⋯⋯ SD, $y/D = 0.0$	− − SD, $y/D = 1.9$
⋯⋯ ND, $y/D = 0.0$	− − ND, $y/D = 1.5$
⋯⋯ UD, $y/D = 0.0$	− − UD, $y/D = 1.0$
⋯⋯ WT, $y/D = 0.0$	− − WT, $y/D = 1.0$
—— Normal distribution	

FIG. 16. Probability density functions of the velocity fluctuations at $x = 10D$. y/D-positions are at the centerline and at the position of maximum negative skewness. The PDFs have been normalized by the incoming velocity rather than the standard deviation, such that the strength of the fluctuations is comparable between the curves.

reference case. The presented measurements compare two common actuator disk configurations with a rotating model at downstream distances up to 30D, which is significantly farther downstream than presently available in the literature.

The results highlight the importance of choosing the right porous disk design. In particular, it is found that for two disks with the same solidity, only one leads to vortex shedding in the wake. The nonuniform disk produces vortex shedding, whereas no such phenomenon is observed in the wake downstream of the uniform disk. Furthermore, the velocity deficit and turbulence intensity profiles differ between the disks. The wake downstream of the nonuniform disk is highly turbulent. The high turbulence intensity increases transport, spreading the wake. On the other hand, the uniform disk has little turbulence in the near wake, but rather sharp velocity gradients. The velocity gradients lead to turbulence production, increasing and maintaining higher turbulence levels in the far wake. Thus, the uniform disk has a smaller wake, with higher velocity deficits and higher turbulence intensity in the far wake. The evolution of velocity deficit and turbulence intensity is also different between the disks. The skewness and kurtosis profiles differ between the two disks, with higher magnitudes in the nonuniform disk wake. The governing physics in the two disk wakes are thus significantly different, and the differences persist throughout the measurement domain up to 30D downstream of the disks.

The wake of the wind turbine is asymmetric, which cannot be replicated by any of the static disks. This asymmetry is present even in far wakes, more prominently for higher-order velocity statistics. Apart from the asymmetry, the uniform disk leads to a wake that is a closer replication of the wind turbine wake. The instantaneous structures and the shape and magnitude of velocity statistics are a better match. The two actuator disks in this study were chosen as examples of disks used in the literature and are not designed to replicate the wake of the

particular wind turbine used in this study. They proved to be good choices to evaluate different flow features in porous disk wakes, giving an overview of different flow physics that must be taken into account in actuator disk design processes. Nonetheless, care must be taken when extrapolating these results to other specific disks, because, as we have illustrated, the wake and its evolution are highly dependent on the geometry.

AUTHOR DECLARATIONS
Conflict of Interest

The authors have no conflicts to disclose.

DATA AVAILABILITY

The data that support the findings of this study are openly available in the NTNU Open Research Data repository at https://doi.org/10.18710/FFELKX.

APPENDIX A: SELF-NORMALIZED WAKE PROFILES

Figures 17 and 18 show the self-normalized velocity deficit and turbulence intensity, respectively. This form of normalization places emphasis on the comparison of the shape of the wakes by effectively removing the magnitude from the comparison. From both Figs. 17 and 18, it is evident that the shape of the UD and WT is generally comparable, at least for $x/D \geq 10$. The ND and SD have
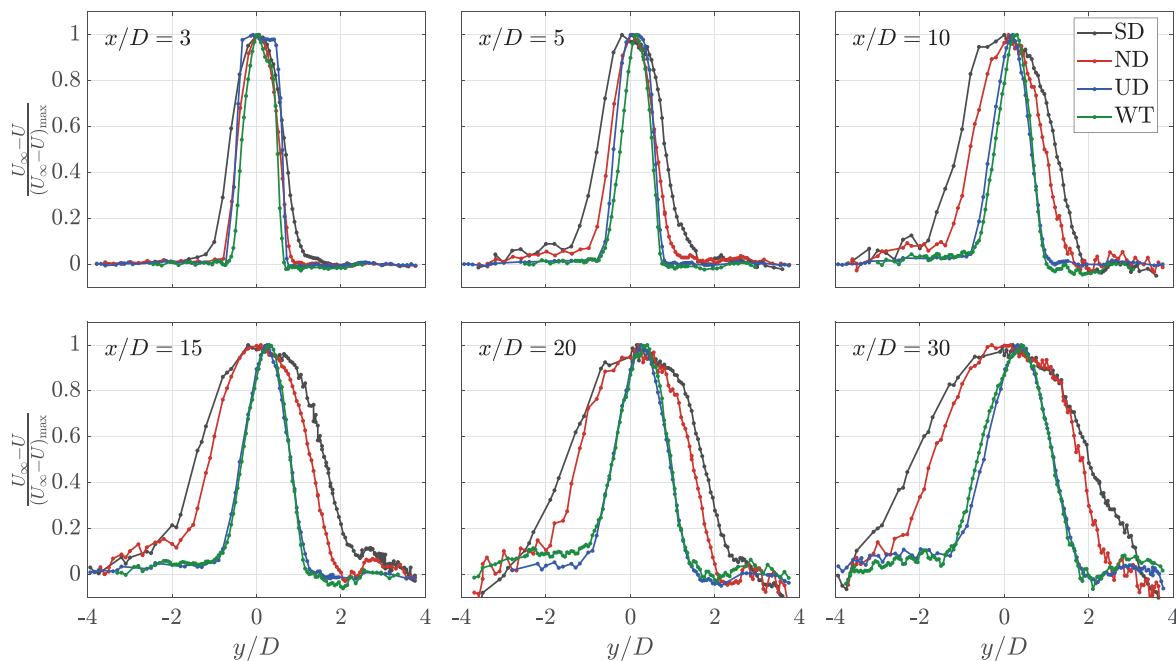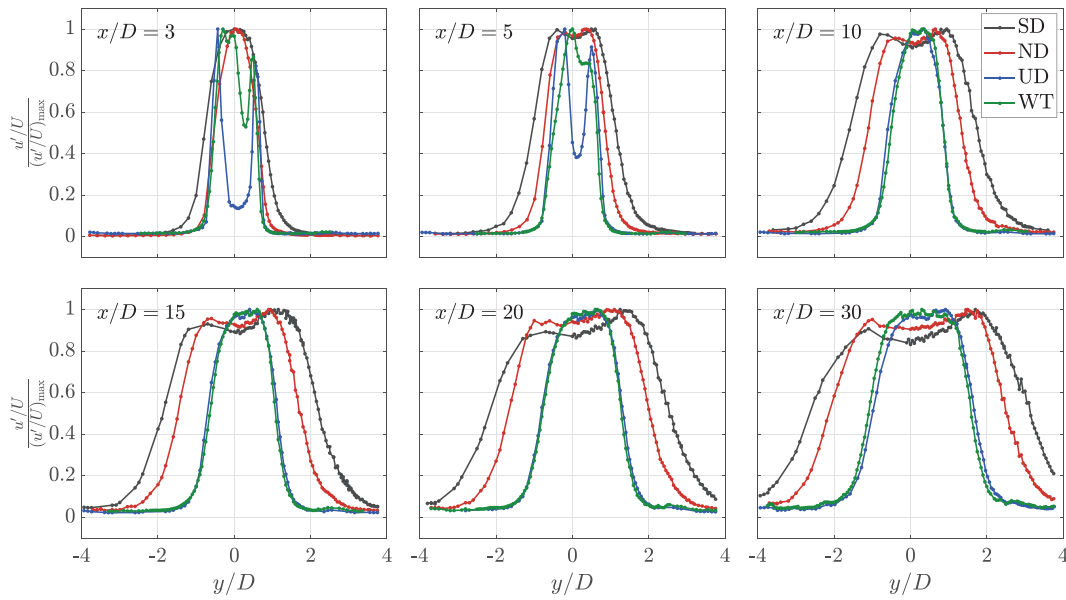

FIG. 17. Self-normalized velocity deficit.

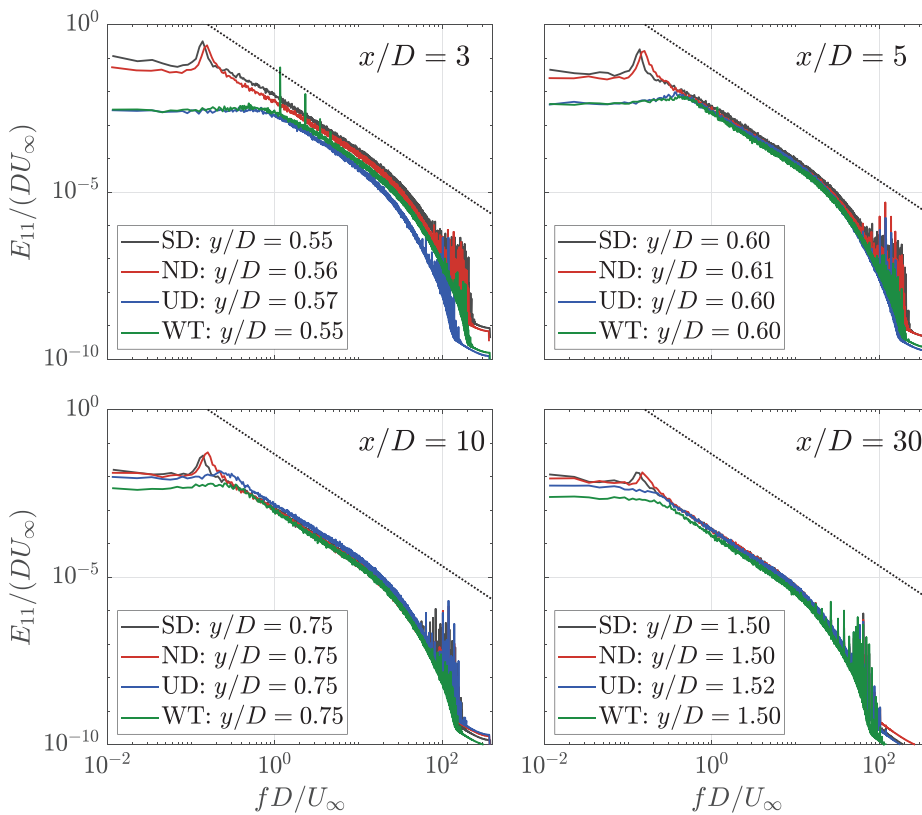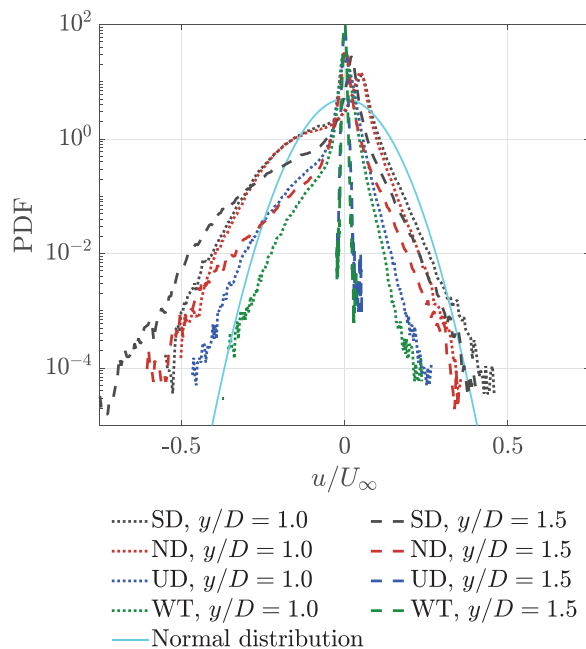**FIG. 18.** Self-normalized turbulence intensity.

FIG. 19. Velocity spectra at different downstream positions. Spectra are taken at a location approximately centered between the position where the velocity deficit is half the maximum velocity deficit for the ND and the UD. The straight solid line represents a reference $f^{-5/3}$ curve.

FIG. 20. Probability density functions of the velocity fluctuations at $x = 10D$. The PDFs have been normalized by the incoming velocity rather than the standard deviation, such that the strength of the fluctuations is comparable between the curves.

distinctively different shapes, generally with a wider wake, but are more comparable to each other than to the UD and WT. These curves complement those provided in the main text where the magnitude is also incorporated.

APPENDIX B: ADDITIONAL VELOCITY SPECTRA AND PDFS

Figure 11 shows the velocity spectra at the position where the velocity deficit is half the maximum velocity deficit. It is also interesting to compare spectra at the same physical position. This is done in Fig. 19, at a position approximately centered between the ND and UD positions in Fig. 11. The two figures show the same energy containing frequencies. There are some small changes in the energy content, but that is to be expected, as the TI differs between the positions. In sum, comparing the spectra as in Fig. 19 does not change the results and conclusions presented in the body of this work.

In the same manner, PDFs plotted at $y/D = 1$ and $y/D = 1.5$ are shown in Fig. 20 to allow a direct comparison at the same physical location. For both y-positions, the streamwise position is $x/D = 10$. At $y/D = 1.5$, the measurement position is outside the UD and WT wakes, and thus the TI is low. Therefore, these positions have very narrow velocity distributions. The clear asymmetry of the other profiles shows the skewness of the flow, while the large tails, in particular, for the SD and ND wakes, show the high kurtosis of the velocity distribution.

REFERENCES

[1]R. J. Barthelmie and L. E. Jensen, "Evaluation of wind farm efficiency and wind turbine wakes at the Nysted offshore wind farm," Wind Energy **13**, 537–586 (2010).

[2]K. Thomsen and P. Sørensen, "Fatigue loads for wind turbines operating in wakes," J. Wind Eng. Ind. Aerodyn. **80**, 121–136 (1999).

[3]L. J. Vermeer, J. N. Sørensen, and A. Crespo, "Wind turbine wake aerodynamics," Prog. Aerosp. Sci. **39**, 467–510 (2003).

[4]D. Medici and P. H. Alfredsson, "Measurements on a wind turbine wake: 3D effects and bluff body vortex shedding," Wind Energy **9**, 219–236 (2006).

[5]W. Zhang, C. D. Markfort, and F. Porté-Agel, "Near-wake flow structure downwind of a wind turbine in a turbulent boundary layer," Exp. Fluids **52**, 1219–1235 (2012).

[6]R. J. Stevens and C. Meneveau, "Flow structure and turbulence in wind farms," Annu. Rev. Fluid Mech. **49**, 311–339 (2017).

[7]F. Porté-Agel, M. Bastankhah, and S. Shamsoddin, "Wind-turbine and wind-farm flows: A review," Boundary Layer Meteorol. **174**, 1–59 (2020).

[8]F. Porté-Agel, Y. T. Wu, and C. H. Chen, "A numerical study of the effects of wind direction on turbine wakes and power losses in a large wind farm," Energies **6**, 5297–5313 (2013).

[9]J. F. Manwell, J. G. McGowan, and A. L. Rogers, *Wind Energy Explained: Theory, Design and Application* (John Wiley and Sons, Ltd., Chichester, UK, 2009).

[10]Y.-T. Wu and F. Porté-Agel, "Large-eddy simulation of wind-turbine wakes: Evaluation of turbine parametrisations," Boundary Layer Meteorol. **138**, 345–366 (2011).

[11]Y.-T. Wu and F. Porté-Agel, "Simulation of turbulent flow inside and above wind farms: model validation and layout effects," Boundary Layer Meteorol. **146**, 181–205 (2013).

[12]S. de Jong Helvig, M. K. Vinnes, A. Segalini, N. A. Worth, and R. J. Hearst, "A comparison of lab-scale free rotating wind turbines and actuator disks," J. Wind Eng. Ind. Aerodyn. **209**, 104485 (2021).

[13]M. Gaumond, P.-E. Réthoré, S. Ott, A. Peña, A. Bechmann, and K. S. Hansen, "Evaluation of the wind direction uncertainty and its impact on wake modeling at the Horns Rev offshore wind farm," Wind Energy **17**, 1169–1178 (2014).

[14]K. S. Hansen, P.-E. Réthoré, J. Palma, B. G. Hevia, J. Prospathopoulos, A. Peña, S. Ott, G. Schepers, A. Palomares, M. P. van der Laan, and P. Volker, "Simulation of wake effects between two wind farms," J. Phys.: Conf. Ser. **625**, 012008 (2015).

[15]P. Argyle, S. Watson, C. Montavon, I. Jones, and M. Smith, "Modelling turbulence intensity within a large offshore wind farm," Wind Energy **21**, 1329–1343 (2018).

[16]P. A. Fleming, A. Ning, P. M. O. Gebraad, and K. Dykes, "Wind plant system engineering through optimization of layout and yaw control," Wind Energy **19**, 329–344 (2016).

[17]J. Meyers and C. Meneveau, "Optimal turbine spacing in fully developed wind farm boundary layers," Wind Energy **15**, 305–317 (2012).

[18]R. J. Stevens, D. F. Gayme, and C. Meneveau, "Large eddy simulation studies of the effects of alignment and wind farm length," J. Renewable Sustainable Energy **6**, 023105 (2014).

[19]J. P. Goit and J. Meyers, "Optimal control of energy extraction in wind-farm boundary layers," J. Fluid Mech. **768**, 5–50 (2015).

[20]J. P. Goit, W. Munters, and J. Meyers, "Optimal coordinated control of power extraction in LES of a wind farm with entrance effects," Energies **9**, 29 (2016).

[21]N. O. Jensen, "A note on wind generator interaction," Technical Report No. Risø-M-2411 (Risø National Laboratory, Roskilde, 1983).

[22]S. Frandsen, R. Barthelmie, S. Pryor, O. Rathmann, S. Larsen, J. Højstrup, and M. Thøgersen, "Analytical modelling of wind speed deficit in large offshore wind farms," Wind Energy **9**, 39–53 (2006).

[23]M. Bastankhah and F. Porté-Agel, "A new analytical model for wind-turbine wakes," Renewable Energy **70**, 116–123 (2014).

[24]P. Doubrawa, R. J. Barthelmie, H. Wang, and M. J. Churchfield, "A stochastic wind turbine wake model based on new metrics for wake characterization," Wind Energy **20**, 449–463 (2017).

[25]W. C. Cheng and F. Porté-Agel, "A simple physically-based model for wind-turbine wake growth in a turbulent boundary layer," Boundary Layer Meteorol. **169**, 1–10 (2018).

[26]M. Bastankhah, B. L. Welch, L. A. Martínez-Tossas, J. King, and P. Fleming, "Analytical solution for the cumulative wake of wind turbines in wind farms," J. Fluid Mech. **911**, 53 (2021).

[27]G. España, S. Aubrun, S. Loyer, and P. Devinant, "Spatial study of the wake meandering using modelled wind turbines in a wind tunnel," Wind Energy **14**, 923–937 (2011).

[28]G. España, S. Aubrun, S. Loyer, and P. Devinant, "Wind tunnel study of the wake meandering downstream of a modelled wind turbine as an effect of large scale turbulent eddies," J. Wind Eng. Ind. Aerodyn. **101**, 24–33 (2012).

[29]Y.-A. Muller, S. Aubrun, and C. Masson, "Determination of real-time predictors of the wind turbine wake meandering," Exp. Fluids **56**, 53 (2015).

[30]M. F. Howland, J. Bossuyt, L. A. Martínez-Tossas, J. Meyers, and C. Meneveau, "Wake structure in actuator disk models of wind turbines in yaw under uniform inflow conditions," J. Renewable Sustainable Energy **8**, 043301 (2016).

[31]A. Abdulrahim, M. T. Akpolat, A. Hassanein, M. Perçin, and O. Uzol, "Effects of inflow boundary layer on the wake of a radially non-uniform porous disk," J. Renewable Sustainable Energy **13**, 033302 (2021).

[32]W. Yu, V. W. Hong, C. Ferreira, and G. A. M. van Kuik, "Experimental analysis on the dynamic wake of an actuator disc undergoing transient loads," Exp. Fluids **58**, 149 (2017).

[33]W. Yu, C. Ferreira, and G. A. van Kuik, "The dynamic wake of an actuator disc undergoing transient load: A numerical and experimental study," Renewable Energy **132**, 1402–1414 (2019).

[34]R. Theunissen, P. Housley, C. B. Allen, and C. Carey, "Experimental verification of computational predictions in power generation variation with layout of offshore wind farms," Wind Energy **18**, 1739–1757 (2015).

[35]J. Bossuyt, M. F. Howland, C. Meneveau, and J. Meyers, "Measurement of unsteady loading and power output variability in a micro wind farm model in a wind tunnel," Exp. Fluids **58**, 1 (2017).

[36]P. M. Sforza, P. Sheerin, and M. Smorto, "Three-dimensional wakes of simulated wind turbines," AIAA J. **19**, 1101–1107 (1981).

[37]S. Cannon, F. Champagne, and A. Glezer, "Observations of large-scale structures in wakes behind axisymmetric bodies," Exp. Fluids **14**, 450 (1993).

[38]H. Higuchi, J. Zhang, S. Furuya, and B. K. Muzas, "Immediate and near wake flow patterns behind slotted disks," AIAA J. **36**, 1626–1634 (1998).

[39]L. E. Myers and A. S. Bahaj, "Experimental analysis of the flow field around horizontal axis tidal turbines by use of scale mesh disk rotor simulators," Ocean Eng. **37**, 218–227 (2010).

[40]M. Lin, C. Xie, M. Yao, and J. Yang, "Study on the near wake of a honeycomb disk," Exp. Therm. Fluid Sci. **81**, 33–42 (2017).

[41]H. Xiao, L. Duan, R. Sui, and T. Roesgen, "Experimental investigations of turbulent wake behind porous disks," in Proceedings of the 1st Marine Energy Technology Symposium, Washington DC (2013).

[42]M. H. Ranjbar, H. Zanganeh Kia, S. A. Nasrazadani, K. Gharali, and J. Nathwani, "Experimental and numerical investigations of actuator disks for wind turbines," Energy Sci. Eng. **8**, 2371–2386 (2020).

[43]M. Huang, C. Ferreira, A. Sciacchitano, and F. Scarano, "Wake scaling of actuator discs in different aspect ratios," Renewable Energy **183**, 866–876 (2022).

[44]L. A. Martínez-Tossas, M. J. Churchfield, and S. Leonardi, "Large eddy simulations of the flow past wind turbines: Actuator line and disk modeling," Wind Energy **18**, 1047–1060 (2015).

[45]N. Simisiroglou, S.-P. P. Breton, and S. Ivanell, "Validation of the actuator disc approach using small-scale model wind turbines," Wind Energy Sci. **2**, 587–601 (2017).

[46]S. Aubrun, S. Loyer, P. Hancock, and P. Hayden, "Wind turbine wake properties: Comparison between a non-rotating simplified wind turbine model and a rotating model," J. Wind Eng. Ind. Aerodyn. **120**, 1–8 (2013).

[47]L. E. Lignarolo, D. Ragni, C. J. Ferreira, and G. J. Van Bussel, "Experimental comparison of a wind-turbine and of an actuator-disc near wake," J. Renewable Sustainable Energy **8**, 023301 (2016).

[48]I. Neunaber, "Stochastic investigation of the evolution of small-scale turbulence in the wake of a wind turbine exposed to different inflow conditions," Ph.D. thesis (Carl von Ossietzky Universität Oldenburg, 2019).

[49]I. Neunaber, M. Hölling, J. Whale, and J. Peinke, "Comparison of the turbulence in the wakes of an actuator disc and a model wind turbine by higher order statistics: A wind tunnel study," Renewable Energy **179**, 1650–1662 (2021).

[50]E. H. Camp and R. B. Cal, "Mean kinetic energy transport and event classification in a model wind turbine array versus an array of porous disks: Energy budget and octant analysis," Phys. Rev. Fluids **1**, 044404 (2016).

[51]E. H. Camp and R. B. Cal, "Low-dimensional representations and anisotropy of model rotor versus porous disk wind turbine arrays," Phys. Rev. Fluids **4**, 024610 (2019).

[52]R. Theunissen and R. Worboys, "Near-wake observations behind azimuthally perforated disks with varying hole layout and porosity in smooth airstreams at high Reynolds numbers," J. Fluids Eng. **141**, 051108 (2019).

[53]S. Aubrun, M. Bastankhah, R. B. Cal, B. Conan, R. J. Hearst, D. Hoek, M. Hölling, M. Huang, C. Hur, B. Karlsen, I. Neunaber, M. Obligado, J. Peinke, M. Percin, L. Saetran, P. Schito, B. Schliffke, D. Sims-Williams, O. Uzol, M. K. Vinnes, and A. Zasso, "Round-robin tests of porous disc models," J. Phys.: Conf. Ser. **1256**, 012004 (2019).

[54]R. W. Fox, A. T. McDonald, P. J. Pritchard, and J. W. Mitchell, *Fluid Mechanics*, 9th ed. (Wiley, 2016).

[55]S. Gambuzza and B. Ganapathisubramani, "The effects of free-stream turbulence on the performance of a model wind turbine," J. Renewable Sustainable Energy **13**, 023304 (2021).

[56]F. Pierella and L. Sætran, "Wind tunnel investigation on the effect of the turbine tower on wind turbines wake symmetry," Wind Energy **20**, 1753–1769 (2017).

[57]M. Hultmark and A. J. Smits, "Temperature corrections for constant temperature and constant current hot-wire anemometers," Meas. Sci. Technol. **21**, 105404 (2010).

[58]J. Bartl and L. Saetran, "Blind test comparison of the performance and wake flow between two in-line wind turbines exposed to different turbulent inflow conditions," Wind Energy Sci. **2**, 55–76 (2017).

[59]L. Zhan, S. Letizia, and G. Valerio Iungo, "LiDAR measurements for an onshore wind farm: Wake variability for different incoming wind speeds and atmospheric stability regimes," Wind Energy **23**, 501–527 (2020).

[60]F. E. Jørgensen, "How to measure turbulence with hot-wire anemometers—A practical guide," Technical Report No. 9040U6154 (Dantec Dynamics, 2005).

[61]C. Santoni, K. Carrasquillo, I. Arenas-Navarro, and S. Leonardi, "Effect of tower and nacelle on the flow past a wind turbine," Wind Energy **20**, 1927–1939 (2017).

[62]J. J. Miau, T. S. Leu, T. W. Liu, and J. H. Chou, "On vortex shedding behind a circular disk," Exp. Fluids **23**, 225–233 (1997).

[63]P. W. Bearman and M. Takamoto, "Vortex shedding behind rings and discs related content vortex shedding behind rings and discs," Fluid Dynamics Research **3**, 1–4 (1988).

[64]C. D. Winant and F. K. Browand, "Vortex pairing: The mechanism of turbulent mixing-layer growth at moderate Reynolds number," J. Fluid Mech. **63**, 237–255 (1974).

[65]M. Kamruzzaman, "On the effects of non-homogeneity on small scale turbulence," Ph.D. thesis (The University of Newcastle, Australia, 2016).

[66]J. Schottler, J. Bartl, F. Mühle, L. Sætran, J. Peinke, and M. Hölling, "Wind tunnel experiments on wind turbine wakes in yaw: Redefining the wake width," Wind Energy Sci. **3**, 257–273 (2018).